Geochimica et Cosmochimica Acta 358 (2023) 38–48

Contents lists available at ScienceDirect

Geochimica et Cosmochimica Acta

journal homepage: www.elsevier.com/locate/gca

Marine barite morphology as an indicator of biogeochemical conditions within organic matter aggregates

Tricia Light [a,*], Francisca Martínez-Ruiz [b], Richard Norris [a]

[a] Scripps Institution of Oceanography, University of California, La Jolla, CA 92037, USA
[b] Instituto Andaluz de la Ciencias de la Tierra (CSIC-UGR), Avda. de las Palmeras 4, 18100 Armilla, Granada, Spain

ARTICLE INFO

Associate editor: Encarnación Ruiz Agudo

Keywords:
Marine barite
Mineral precipitation
Crystal morphology
Organic matter aggregates
Remineralization

ABSTRACT

Marine barite is commonly used as a proxy to reconstruct past ocean productivity. Its distribution in the water column mirrors organic carbon fluxes since it precipitates within microenvironments in decomposing organic matter aggregates. Barite and barium proxies are therefore used to study various aspects of organic matter remineralization and the marine carbon cycle. Barite naturally occurs in a wide variety of crystal sizes and morphologies, but barite crystals that form in the ocean water column are dominantly 1–2 μm in length and have barrel-shaped morphologies. Here, we conducted a series of laboratory experiments to determine the physical and chemical conditions that yield barite crystals similar to marine barite. We found that barite saturation index, the presence and identity of organic compounds, and experiment duration all exert a strong influence on barite crystal size and morphology. Barrel-shaped, 1 μm length crystals resembling marine barite were produced in experiments with a barite saturation index of 2.5, soy phospholipid concentrations of $\geq$50 mg L^{-1}, and experiment durations of $\leq$10 min. These findings help constrain the plausible biogeochemical conditions within the aggregate microenvironments in which marine barite precipitates. Relatively high experimental concentrations of phospholipids are consistent with the hypothesized involvement of extracellular polymeric substances in marine barite precipitation. Short experiment durations suggest that a favorable saturation state may be short-lived in marine organic matter aggregates. We present detailed mineralogical and crystallographic analyses of the crystals we synthesized to gain insight into barite crystal growth. This work deepens our understanding of the mechanisms behind marine barite precipitation and sheds light on microscale spatial and temporal dynamics within organic matter aggregates.

1. Introduction

The association of particulate Ba and particulate organic carbon in the ocean water column has been broadly demonstrated (e.g., Bishop, 1988; Dehairs et al., 1980). Since marine barite precipitates mostly within sinking and suspended particulate matter, it can be a useful tool for studying the remineralization of marine organic matter aggregates such as fecal pellets and marine snow (Carter et al., 2020; Yao et al., 2021 and references therein). The gravitational settling of organic particles transports an estimated 7.3 $\times$ 10^{15} g C out of the surface ocean each year (Nowicki et al., 2022), so understanding marine particle dynamics is central to our ability to constrain the global carbon cycle (Hülse et al., 2017). However, studying marine organic matter aggregates, particularly in situ, is logistically challenging. Important questions remain regarding marine organic matter aggregate formation, persistence, and decomposition in the past and present, and this makes it difficult to predict how marine ecosystems will respond to future anthropogenic climate change (Buesseler et al., 2020; Fakhraee et al., 2020; Henson et al., 2022). Ba proxies have the potential to provide new insights into these processes because marine barite is relatively well-preserved in ocean sediments (Bishop, 1988; Paytan et al., 1998), and barite abundance in sediments can be fairly easily measured through methods such as sequential leaching (Paytan et al., 1996) or chelating ligand analysis (House and Norris, 2020). Sediment barium concentrations can also be easily measured (e.g., Murray and Leinen, 1993).

The ocean is largely undersaturated with respect to barite (Monnin et al., 1999), but marine barite has been demonstrated to precipitate in supersaturated microenvironments within decomposing organic matter aggregates (Bishop, 1988; Ganeshram et al., 2003). The precise mechanism behind the formation of these supersaturated microenvironments

* Corresponding author.
E-mail address: tlight@ucsd.edu (T. Light).

https://doi.org/10.1016/j.gca.2023.08.012
Received 13 December 2022; Accepted 12 August 2023
Available online 15 August 2023

is still unclear, but recent work suggests that phospholipids contained by the extracellular polymeric substances (EPS) in organic matter aggregates may play an important role in bioaccumulating barium. Barium has been shown to bind to phosphate groups on cell surfaces and within EPS under experimental conditions (Martinez-Ruiz et al., 2018). Similar crystallization pathways have been observed in the ocean water column, where barite is particularly abundant in suspended organic matter at intermediate depths in the mesopelagic zone (Martinez-Ruiz et al., 2020; Martinez-Ruiz et al., 2019). A portion of this barite then accumulates in marine sediments, where it is well-preserved under non sulfate-reducing conditions (e.g., Paytan et al., 1998).

Because marine barite precipitation is closely linked to organic matter decomposition, the accumulation rate of barite in marine sediments is broadly used as a proxy for the export of organic carbon out of the surface ocean (e.g., Carter et al., 2016; Erhardt et al., 2013; Kim et al., 2022; Lowery and Bralower, 2022; Ma et al., 2014; Paytan et al., 1996). Barite abundance and barium isotopes within the water column are used as proxies for modern mesopelagic organic carbon remineralization (e.g., Jacquet et al., 2011; Hsieh and Henderson, 2017). Sediment marine barite also serves as an archive for past seawater sulfur, oxygen, and strontium isotopes (e.g., Markovic et al., 2016; Paytan et al., 1993; Yao et al., 2020). However, uncertainties in the specifics of marine barite formation often complicate the interpretation of sediment barite records. For instance, periods of high barite accumulation at certain locations following the Cretaceous-Paleogene mass extinction (Lowery and Bralower, 2022) or during Eocene hyperthermals (Griffith et al., 2021) may represent increases in carbon export, but they may also be partly due to changes in other ecosystem parameters such as plankton community composition and intensity of organic matter remineralization.

Despite the widespread utility of marine barite proxies, relatively little work has focused on the processes that cause marine barite precipitation and on how marine barite crystal size and morphology can shed light on the organic matter aggregates in which barite forms. Barite naturally occurs in a wide range of sizes and morphologies across different environments (Goldschmidt, 1913), but marine barite crystals show distinct morphologies that tend to be barrel-shaped, elliptical, or six-sided and approximately 1 μm in length (Fig. 1) (Bertram and Cowen, 1997; Light and Norris, 2021; Sun et al., 2015). Previous laboratory investigations into barite precipitation have shown that barite crystal size and morphology is determined by factors such as barite saturation index, Ba^{2+} to SO_4^{2-} ratio, solution mixing protocol, concentration of Na^+ and other cations, and the presence of organic compounds such as sodium formate, ethylenediaminetetraacetic acid (EDTA), benzoic acids, polyacrylic acid, humic acids, and phosphonates (Benton et al., 1993; Bernard-Michel et al., 2002; Fernandez-Diaz et al., 1990; Freeman et al., 2006; Godinho and Stack, 2015; Jones and Ogden, 2009; Judat and Kind, 2004; Kowacz et al., 2007; Ruiz-Agudo et al., 2015; Ruiz-Agudo et al., 2016; Qi et al., 2001; Shen et al., 2007; Smith et al., 2004; Widanagamage et al., 2014; Widanagamage et al., 2018). Crystal nucleation that is homogeneous (in solution) vs. heterogeneous (on surfaces) may also impact barite crystal size and morphology (Deng et al., 2019; He et al., 1995, Yuan et al., 2021). However, most prior studies on barite morphology were not designed to emulate marine environments and did not reliably produce crystals resembling marine barite.

Recent work has shown that barite crystals resembling marine barite can result from a two-step process in which a Ba-P amorphous phase formed with phytic acid is exposed to a sulfate-bearing solution (Ruiz Agudo et al., 2021). Boon and Jones (2016) investigated the elemental composition of barite crystals formed in synthetic seawater solutions, but the crystals they produced generally did not resemble marine barite

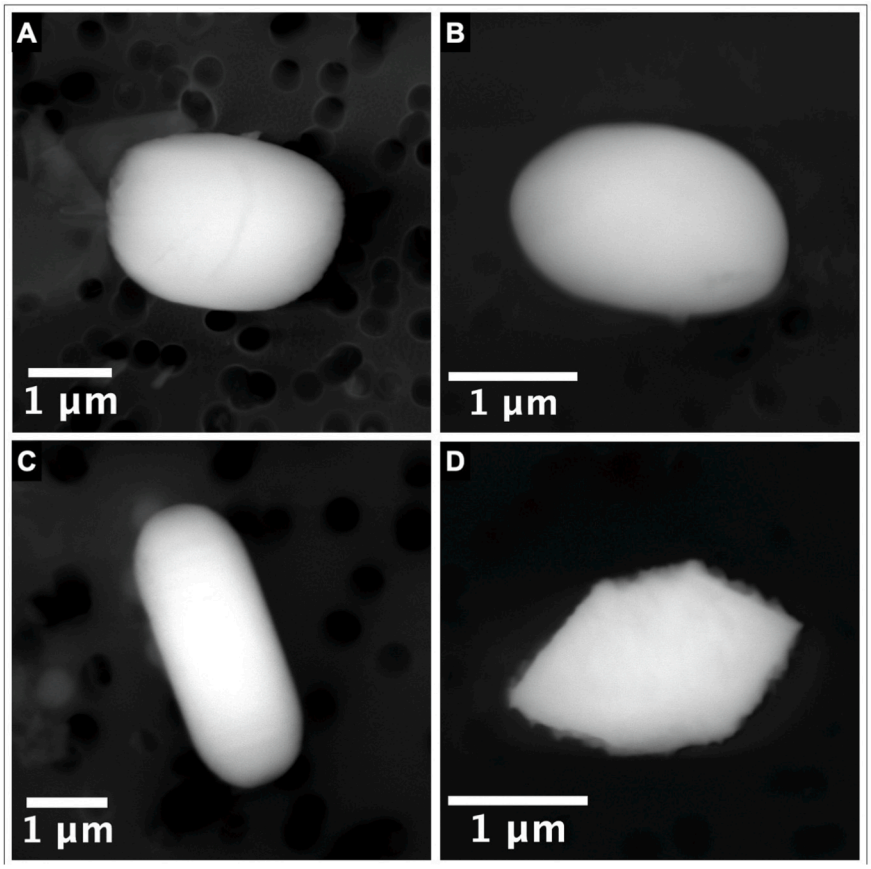

Fig. 1. Representative marine barite crystals collected from a water depth of 200 m in the North Pacific. A), B), and C) Typical elliptical or barrel-shaped barite crystals. D) Six-sided barite crystal with irregular edges. See Light and Norris, 2021 for detailed information regarding crystal collection and analysis.

in size or morphology. Rather, marine barite morphologies resemble that of some carbonates resulting from microbially mediated precipitation (Dupraz et al., 2009). In the case of carbonates, mineral species abundance and morphology provides information on the conditions of precipitation such as the nature of the mediating biofilm and concentrations of organic compounds such as polyaspartic acid and other polyamino acids (e.g., Braissant et al., 2003). Thus, barite morphology may shed light on the organic microenvironments in which barite forms in natural settings.

Here, we conducted a wide variety of laboratory experiments to identify conditions that produce marine barite's characteristic size and morphology. We use these findings to constrain plausible biogeochemical conditions within the organic matter aggregate microenvironments in which marine barite precipitates in the ocean water column. We also explore the implications of marine barite morphology for both barite crystal growth and the marine barium cycle.

2. Materials and methods

2.1. Barite precipitation protocol

We conducted a series of laboratory experiments to assess the role of barite saturation index, presence and concentration of organic additives, and experiment duration time on barite crystal morphology (Table 1). All solutions were made using ultrapure Milli-Q water (18.2 MΩ·cm). Experiments were designed to simulate the relative concentrations of seawater constituents as closely as possible.

Barite supersaturation was obtained through the addition of barium chloride ($BaCl_2$, Fisher Scientific) and sodium sulfate (Na_2SO4, Fisher Scientific) to maintain a 1:625 $[Ba^{2+}]$:$[SO_4^{2-}]$ ratio, or the ratio achieved when the SO_4^{2-} concentration in solution is equal to that of seawater and Ba^{2+} is enriched to achieve a saturation index of 2.5 (Emerson and Hedges, 2008). Barite saturation indices were calculated using The Geochemist's Workbench software (Bethke, 2022). Strontium nitrate ($SrNO_3$, Sigma-Aldrich) was added to each solution to achieve a $[Ba^{2+}]$:$[Sr^{2+}]$ ratio of 1. Sodium chloride (NaCl, Innovating Science) was added to all experiments as necessary to achieve $[Na^+] = 460$ mM to approximate seawater Na^+ concentrations (Emerson and Hedges, 2008). One exception was made for the pyromellitic acid experiment; pyromellitic acid was observed to form a precipitate in the presence of Na^+, so NaCl was not added to this solution and the concentrations of all other species were adjusted accordingly. Additional experiments were conducted to assess the influence of $[Ba^{2+}]$:$[Sr^{2+}]$ and $[Ba^{2+}]$:$[SO_4^{2-}]$ and ratios on barite crystal morphology (Fig. SI, SII).

We used four organic additives in our experiments: sodium formate (HCOONa), L-ascorbic acid ($C_6H_8O_6$), pyromellitic acid (1,2,4,5-benzenetetracarboxylic acid, $C_{10}H_6O_8$), and EDTA ($C_{10}H_{16}N_2O_8$). These additives were acquired from Sigma-Aldrich, TCI, Sigma-Aldrich, and Eisen-Golden, respectively. Sodium formate was selected because formic acid occurs naturally in seawater (Koyama and Thompson, 1964), and sodium formate has been previously shown to produce elliptical barite crystals (Widanagamage et al., 2018). Experiments with L-ascorbic acid were run because it also occurs naturally in seawater (Wangersky, 1952) and has been shown to produce spherical calcium carbonate crystals (Saraya, 2015). Pyromellitic acid was employed because it has been previously shown to produce elliptical barite crystals (Freeman et al., 2006), and benzoic acids can be used as a proxy for carboxy-rich alicylic molecules, which are a main component of marine dissolved organic matter (Liu et al., 2020). EDTA was used because it has been previously shown to produce elliptical barite crystals, and there is a large body of literature on the interactions between EDTA and barite (e.g., Akyol and Cedimagar, 2016; Jones et al., 2007; Liu et al., 2018; Widanagamage et al., 2018; Zhang et al., 2011). EDTA also forms complexes with Ba^{2+} ions in solution, so the EDTA experiment was conducted at higher calculated barite supersaturation to compensate for complexed ions (Jones et al., 2007). Soy phospholipids were acquired from Millipore Sigma and contained roughly equal amounts of lecithin, cephalin, and phosphatidylinositol with minor amounts of other phospholipids and polar lipids. Soy phospholipids were used because phospholipids have been hypothesized to play an important role in marine barite precipitation (Martinez-Ruiz et al., 2018, 2019).

Experiments were designed to minimize contamination and high barite saturation indices at the solution mixing interface. All glassware was cleaned in 5% hydrochloric acid overnight. All reactants except Na_2SO_4 were dissolved in 40 ml water in a 200 ml glass beaker. Soy phospholipids were sonicated to dissolution in 5 ml of ethanol before addition to this $BaCl_2$ solution. Na_2SO_4 was separately dissolved in 10 ml of water. The $BaCl_2$ solution was then rapidly stirred on a magnetic stir plate while the Na_2SO_4 solution was slowly added. The final solution was then removed from the stir plate and allowed to sit for the specified time in the experimental treatment. The solution was then syringe filtered through a 0.2 μm pore size, 25 mm diameter nylon membrane filter enclosed in a reusable filter holder. Filters were then dried in a 60 ℃ oven overnight prior to analysis. All experiments were conducted in duplicate.

We initially conducted experiments in polycarbonate plastic bottles, but we found that these bottles retained nuclei of barite crystals through repeated acid washes. These retained nuclei influenced the size and morphology of barite crystals synthesized in later experiments and led to inconsistent results between duplicate experiments. We also pursued many iterations of the solution mixing protocol before we discovered the importance of minimizing high barite saturation indices at the solution

Table 1
Experimental parameters, analyses conducted, and resultant barite crystal morphologies. SI is the saturation index, while other experiments focused on varying concentrations of organic additives and experiment duration times. All Soy and Time treatments also contained 9 % v/v ethanol.

Treatment	$BaSO_4$ SI	Organics	Time (minutes)	Analyses	Dominant Crystal Morphology
SI-1.5	1.5	None	2	SEM	Irregular
SI-2	2	None	2	SEM, HRTEM	Irregular
SI-2.5	2.5	None	2	SEM, HRTEM	Rectangular, rhomboidal
SI-3	3	None	2	SEM	Concave diamond, rosette
SI-3.5	3.5	None	2	SEM	Concave diamond, rosette
Formic	2.5	1 M formic acid	2	SEM, HRTEM	Globular elliptical
Ascorbic	2.5	1 M ascorbic acid	2	SEM, HRTEM	Rectangular, hollow rhomboidal
Pyromellitic	2.5	48 mM pyromellitic acid	2	SEM, HRTEM	Elliptical, rhomboidal
EDTA	3	25 mM EDTA	2	SEM, HRTEM	Elliptical
Ethanol	2.5	9 % v/v ethanol	2	SEM	Rectangular, rhomboidal
Soy-10	2.5	10 mg L^{-1} soy phospholipids	2	SEM	Rectangular, rhomboidal, irregular
Soy-50	2.5	50 mg L^{-1} soy phospholipids	2	SEM	Elliptical, irregular
Soy-100	2.5	100 mg L^{-1} soy phospholipids	2	SEM, HRTEM	Elliptical
Soy-200	2.5	200 mg L^{-1} soy phospholipids	2	SEM, HRTEM	Elliptical
Time-10	2.5	100 mg L^{-1} soy phospholipids	10	SEM, HRTEM	Elliptical, globular
Time-30	2.5	100 mg L^{-1} soy phospholipids	30	SEM, HRTEM	Globular
Time-120	2.5	100 mg L^{-1} soy phospholipids	120	SEM, HRTEM	Globular

mixing interface. These iterations included adding concentrated $BaCl_2$ to a dilute SO_4^{2-} solution, adding dilute $BaCl_2$ to the Na_2SO_4 solution without stirring, and scaling the experimental protocol up to larger volumes.

2.2. Barite crystal analyses

Morphology assessments of each treatment were conducted via Scanning Electron Microscopy equipped with Energy-dispersive X-ray Spectroscopy (SEM-EDX). One quarter of each nylon membrane filter was mounted on an aluminum stub with carbon tape for analysis. Size analysis and morphological characterization were conducted on a Phenom Desktop SEM with an accelerating voltage of 15 kV and working distance of 9–10 mm (Scripps Institution of Oceanography, UCSD). A backscatter electron (BSE) detector was used to identify likely barite crystals, and their identity was confirmed by EDX. Dominant crystal morphologies for each treatment were determined based on the visual assessment of at least 20 barite crystals on each duplicate filter. Higher-quality images of representative crystals were then acquired using an AURIGA FIB- FESEM Carl Zeiss SMT microscope equipped with EDX and operated at 10 kV (Centre for Scientific Instrumentation, University of Granada) and a FEI Apreo 2 LoVac SEM equipped with EDX and operated at 20 kV (NanoEngineering Materials Research Center, University of California San Diego). Images were processed using the FIJI distribution of ImageJ (Schindelin et al., 2012; 2015).

Barite crystals from treatments Soy-100, Time-10, Time-30, and Time-120 (with experiment duration times of 2, 10, 30 and 120 min, respectively) were quantitatively analyzed to determine the effect of experiment duration on crystal size. Twenty barite crystals for each treatment were randomly selected and imaged during SEM analysis. Images were then analyzed using the FIJI distribution of ImageJ (Schindelin et al., 2012; 2015). Scaling parameters were extracted from the metadata of each image. Barite crystals were distinguished from the filter background using the Trainable Weka Segmentation plugin (Arganda-Carreras et al., 2017). Barite crystal areas were then calculated using FIJI's Analyze Particles plugin. Results were plotted in R using ggplot 2.0 (R Core Team, 2020; Wickham, 2016).

Eleven of the seventeen experimental treatments were selected for additional analysis via high-resolution transmission electron microscopy (HRTEM) (Table 1). For each of these treatments, one quarter of one duplicate filter was suspended in ethanol and ground with an agate mortar. Particulate matter suspended in this ethanol was then deposited on carbon-film-coated copper grids. Barite crystals on these grids were then imaged using a FEI TITAN G2 60–300 microscope with a high brightness electron gun (X-FEG) operated at 300 kV and equipped with a Cs image corrector CEOS (Center for Scientific Instrumentation, University of Granada). Elemental composition maps were acquired using a SUPER-X silicon-drift windowless EDX detector. Spot EDX spectra were semi-quantitatively analyzed to determine the relative intensities of phosphorous across soy phospholipid treatments (Table SI). Selected area electron diffraction (SAED) patterns were also collected on barite crystals. Two to four crystals were imaged for each treatment in which HRTEM analysis was conducted. SAED patterns were quantitatively analyzed using CrysTBox Software (Klinger, 2017). Since a greater number of crystals were analyzed via SEM and HRTEM sample preparation preferentially selects for small crystals, SEM was used to determine the dominant crystal morphologies and size distributions for each treatment.

3. Results

3.1. Effect of saturation index on barite morphology

Barite saturation index (SI) had a large effect on observed barite crystal morphology. Barite crystals precipitated in solutions with a barite SI of 1.5 and 2 displayed irregular morphologies and were mostly under 1 μm in length (Fig. 2A, 2B). Barite crystals from solutions of SI 2.5 displayed clearly defined rectangular and rhomboidal morphologies and were 1–3 μm in length (Fig. 2C). Solutions of SI 3 and 3.5 produced crystals with distinctive twinned concave diamond and bladed rosette morphologies ranging from 1 μm to 5 μm in length (Fig. 2D, 2E). These morphologies were consistent with those observed under similar conditions in Godinho and Stack (2015). Solution mixing protocol had a large effect on barite precipitation; in early experiments that did not minimize barite concentration gradients at the solution mixing interface, crystal morphologies typical of SI 3 and 3.5 were observed even in solutions with lower saturation indices. $[Ba^{2+}]$:$[Sr^{2+}]$ had no discernible effect on barite crystal size and morphology within the range of conditions tested here (Fig. SI). $[Ba^{2+}]$:$[SO_4^{2-}]$ had little effect on barite crystal size and morphology, but crystals precipitated at very high $[SO_4^{2-}]$ were smaller and displayed rounded corners (Fig. SII).

3.2. Effect of organic additives on barite morphology

Various organic additives had distinct effects on barite crystal morphology. In experiments with barite saturation of 2.5, formic acid produced crystals with globular, pointed elliptical morphologies, visibly uneven surface textures, and lengths of 1–3 μm (Fig. 3A). Ascorbic acid, with SI = 2.5, produced rectangular and rhomboidal crystals with lengths mostly under 1 μm (Fig. 3B). Approximately half of the rhomboidal crystals contained center holes resembling dissolution pits (Fig. 3B). Pyromellitic acid, with SI = 2.5, produced rectangular and narrow elliptical crystals mostly under 1 μm in length (Fig. 3C). Finally, EDTA (SI = 3) produced broad, elliptical crystals 1–2 μm in length (Fig. 3D).

HRTEM results were generally consistent with SEM observations (Fig. 3E, 3H), but HRTEM images for Ascorbic and Pyromellitic treatments showed more irregular morphologies than those observed during SEM analysis (Fig. 3F, 3G). Elemental composition maps for crystals synthesized in the presence of all four organic additives were consistent with barite (Fig. 3I-L). Lattice-fringe images and SAED patterns for all four treatments yielded d-space measurements consistent with barite (Fig. 3M-T). All four SAED patterns showed well-defined crystallinity, with the Formic treatment displaying some polycrystalline character (Fig. 3N, 3P, 3R).

3.3. Effect of soy phospholipids on barite morphology

Barite crystals similar to marine barite formed in the presence of moderately high concentrations of soy phospholipids. Barite crystals precipitated in the presence of only ethanol or ethanol and 10 mg L^{-1} soy phospholipids displayed regular rectangular and rhomboidal morphologies like those precipitated without soy phospholipids (Fig. 4A, 4B). However, crystals precipitated with ethanol and 50, 100, and 200 mg L^{-1} soy phospholipids displayed largely elliptical morphologies (Fig. 4C-E). Most barite crystals for all four treatments were 1–2 μm in length.

HRTEM analysis of barite in the absence of soy phospholipids confirmed its well-defined euhedral morphology (Fig. 4F). HRTEM analysis of 100 and 200 mg L^{-1} soy phospholipid treatments showed crystals that were broadly elliptical but fairly irregular in shape (Fig. 4L and 4R). Elemental composition maps were consistent with barite (Fig. 4G, 4H, 4M, 4N, 4S, 4T). Crystals from SI-2.5, Soy-100, and Soy-200 treatments showed some phosphorous incorporation into the crystal lattice, but the inclusion of phosphorous did not appear to increase with increasing concentrations of phospholipids in solution (Fig. 4I, 4O, 4U). Semi-quantitative analysis of spot EDX spectra suggest greater incorporation of phosphorous in the Soy-100 treatment than the other two treatments (Table SI). Lattice-fringe images and SAED patterns for all three treatments showed well-defined crystallinity and yielded d-space measurements consistent with barite (Fig. 4J, 4K, 4P, 4Q, 4V, 4W).

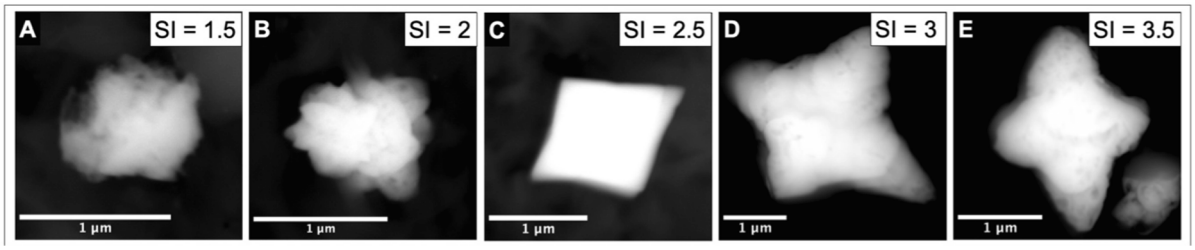

Fig. 2. SEM images of representative barite crystal morphologies for treatments A) SI-1.5, B) SI-2, C) SI-2.5, D) SI-3, and E) SI-3.5.

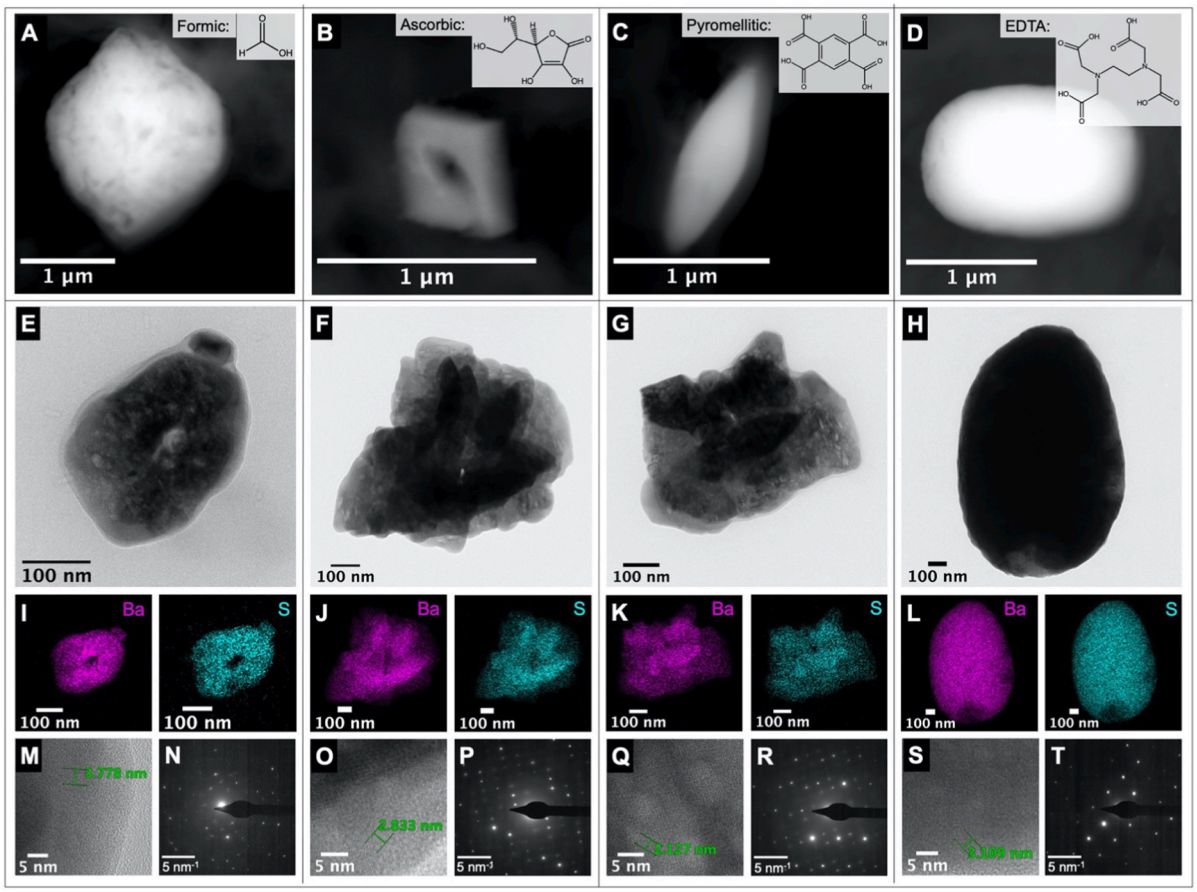

Fig. 3. SEM images of representative barite crystal morphologies for treatments A) Formic, B) Ascorbic, C) Pyromellitic, and D) EDTA. Insets depict the chemical structure of the corresponding organic compound. HRTEM images of crystals from E) Formic, F) Ascorbic, G) Pyromellitic, and H) EDTA treatments. Ba and S elemental composition maps of corresponding crystals for I) Formic, J) Ascorbic, K) Pyromellitic, and L) EDTA treatments. Lattice fringe images and SAED patterns for a region of the corresponding crystal for M) and N) Formic, O) and P) Ascorbic, Q) and R) Pyromellitic, and S) and T) EDTA treatments. Lattice-fringe images show d-spacings characteristic of barite: 3.77 Å (201) for M, 2.84 Å (112) for O, 2.12 Å (113) for Q, and 3.10 Å (211) for S. Ten unit cells have been measured, so the indicated measurements in nm correspond to d-spacings in Å.

3.4. Effect of experiment duration on barite morphology

Barite crystals synthesized in the presence of 100 mg L^{-1} soy phospholipids became larger and more irregularly shaped with longer experiment durations (Figs. 5, 6). Crystals in solutions allowed to react for 2 min displayed regular elliptical morphologies and had an average length of 0.8 ± 0.1 µm (Figs. 5A, 6). Barite crystals became more globular with increasing experiment duration times and reached average lengths of 2.7 ± 0.4 µm, 15 ± 2 µm, and 54 ± 8 µm after 10, 30, and 120 min, respectively (Figs. 5B-D, 6). D-spacing measurements from lattice-fringe images for crystals from 2-, 10-, and 30-minute treatments are consistent with barite. Lattice-fringe images and SAED patterns showed increasing polycrystallinity with longer experiment durations (Fig. 5E-J).

4. Discussion

4.1. Barite morphology as an indicator of conditions within organic matter aggregates

Our results show that barite saturation index, the presence of organic compounds, and experiment duration determine barite crystal size and morphology. Since only four out of the seventeen experiments we conducted here yielded barite crystals that resemble characteristic marine barite crystals (Table 1, Fig. 7), we can use our findings to constrain likely biogeochemical conditions in the organic matter aggregate microenvironments in which barite precipitates. Microscale dynamics within organic matter aggregates are poorly constrained, despite the importance of aggregates to marine ecosystems and the marine carbon

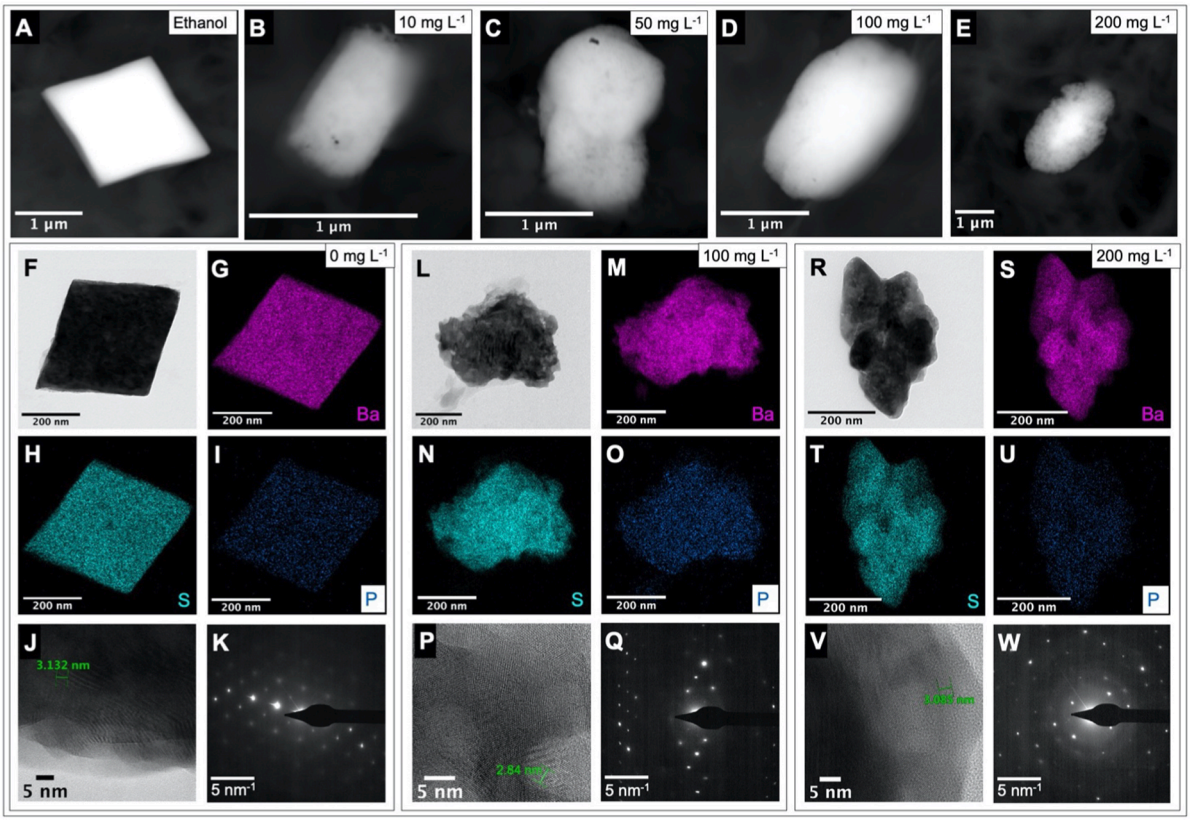

Fig. 4. SEM images of representative barite crystal morphologies for treatments A) Ethanol, B) Soy-10, C) Soy-50, D) Soy-100, and E) Soy-200. HRTEM images and corresponding elemental composition maps for treatments F-I) SI-2.5, L-O) Soy-100, and R-U) Soy-200. Lattice-fringe images and SAED patterns for a region of the corresponding crystal for J) and K) SI-2.5, P) and Q) Soy-100, and V) and W) Soy-200 treatments. Lattice-fringe images show d-spacings characteristic of barite: 3.10 Å (211) for J, 2.84 Å (112) for P, and 3.10 Å (211) for V. Ten unit cells have been measured, so the indicated measurements in nm correspond to d-spacings in Å.

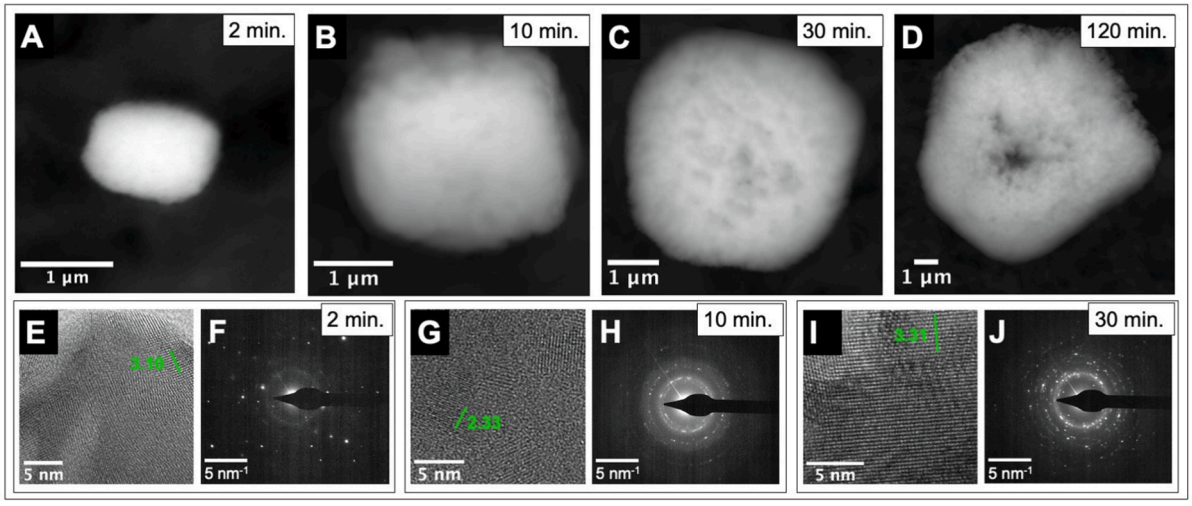

Fig. 5. SEM images of representative barite crystal morphologies for treatments A) Soy-100, B) Time-10, C) Time-30, and D) Time-120. Lattice-fringe images and SAED patterns for crystals from treatments E) and F) Soy-100, G) and H) Time-10, and I) and J) Time-30. Lattice-fringe images show d-spacings characteristic of barite: 3.10 Å (211) for E, 2.33 Å (220) for F, and 3.32 Å (102) for G. Ten unit cells have been measured, so the indicated measurements in nm correspond to d-spacings in Å.

cycle (Iversen, 2023). Therefore, these findings provide new insights into the plausible biogeochemistry of aggregates.

Marine barite crystals likely precipitate within microenvironments in which Ba^{2+} and/or SO_4^{2-} concentrations are high enough to achieve a barite saturation index of around 2.5. Barite crystals that formed in less saturated solutions were small and irregular in shape (Fig. 2A, 2B) compared to most marine barite crystals (Fig. 1). Conversely, solutions with saturation indices above 2.5 produced distinctive concave diamond and rosette morphologies typical of rapid, diffusion-limited crystal growth (Fig. 2D, 2E) (Dirksen and Ring, 1991; Garcia-Ruiz, 1999). Crystals that formed under barite supersaturation of 3 or 3.5 did display rounded corners, which suggests a transition to slower, spiral crystal

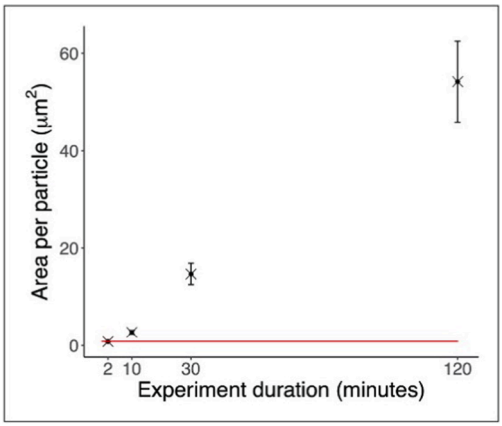

Fig. 6. Average barite crystal area with experiment duration. The red line shows average barite crystal area for marine barite crystals collected from the North Pacific (Light and Norris, 2021).

growth once ongoing barite precipitation lowers the barite supersaturation of the solution (Kucher et al., 2006; Weber et al., 2021). However, these rounded corners were only observed in the presence of diamond and rosette morphologies that, to the best of our knowledge, have never been observed for marine barite crystals (e.g., Dehairs et al., 1980; Light and Norris, 2021). Thus, our findings suggest that whatever mechanism (s) facilitate marine barite precipitation do so by establishing a fairly narrow range of Ba^{2+} and SO_4^{2-} concentrations that allow for stable barite crystal growth. The rarity of irregular crystals in populations of marine barite crystals suggests either that precipitation is inhibited below a SI of ~2.5 or that these crystals form but then dissolve in the water column. Ongoing marine barite precipitation within microenvironments likely prevents sufficient Ba^{2+} and SO_4^{2-} accumulation to establish saturation indices above 2.5.

We did not observe elliptical or barrel-shaped barite crystals resembling marine barite in any experimental treatment without organic compounds. Previous studies have found that high concentrations of Sr^{2+} can enhance barite crystal growth in the [0 1 0] direction and favor the formation of celestite-like morphologies that may more closely resemble marine barite (Weber et al., 2018; Sánchez-Pastor et al., 2006). However, we observed rectangular and rhomboidal barite crystal morphologies even at a Sr^{2+}:Ba^{2+} ratio of 10:1 under our experimental conditions, which were designed to emulate plausible conditions within a marine organic matter aggregate (Fig. S1). Therefore, elevated Sr^{2+} concentrations in organic matter aggregates are unlikely to be the main driver of elliptical marine barite morphologies. Similarly, literature suggests that curvilinear barite crystal morphologies may be promoted by Ba^{2+}:SO_4^{2-} ratios greater than ~5 (Bracco et al., 2016), but these high ratios have little relevance to marine systems given the high ambient concentration of SO_4^{2-} in seawater (28.2 mmol kg^{-1}; Emerson and Hedges, 2008). We explored barite precipitation at barite supersaturation of 2.5 with Ba^{2+}:SO_4^{2-} ratios ranging from elevated Ba^{2+} and ambient seawater SO_4^{2-} (1:625) to ambient seawater Ba^{2+} and elevated SO_4^{2-} (1:6670) (Fig. S2). These experiments did show changes in crystal size and morphology that suggest that Ba^{2+}:SO_4^{2-} ratios affect barite crystal growth mechanisms, but none of these treatments yielded crystals that resemble marine barite in size and morphology (Fig. S2).

Our findings suggest that marine barite crystals precipitate in the presence of phospholipids or other organic compounds. We found that various organic compounds affected barite crystal morphologies, but, of the compounds analyzed here, only EDTA and soy phospholipids produced barite crystals that resembled marine barite (Figs. 3, 4). It is likely that other organic compounds also produce elliptical barite morphologies, but an exhaustive assessment of these compounds is outside the scope of this study. EDTA does not naturally occur in the ocean (Oviedo and Rodríguez, 2003). Thus, the distinctive morphologies of marine barite cannot be attributed to growth modification by EDTA.

Phospholipids have more relevance than EDTA to marine contexts. Soy phospholipids were selected to serve as a proxy for the diverse range of phospholipids produced by marine organisms. Phospholipids in marine EPS are hypothesized to facilitate marine barite precipitation via the bioaccumulation of Ba and formation of amorphous, phosphorus-rich barite precursors (Martinez-Ruiz et al., 2018, 2019). Sulfate groups are then thought to substitute for the phospholipid phosphate moieties in the amorphous precursor, which yields crystalline barite (Martinez-Ruiz et al., 2018, 2019). Amorphous Ba-P phases and short-lived barite precursors have also been observed in other laboratory investigations (e.g., Jones, 2012; Ruiz-Agudo et al., 2020; Ruiz Agudo et al., 2021). Given this existing literature, it is notable that phospholipid experimental treatments produced barite crystals that resemble marine barite. With the relatively high barite supersaturation of these treatments, phospholipid Ba bioaccumulation was not necessary to yield barite precipitation. However, barite precipitation in these treatments

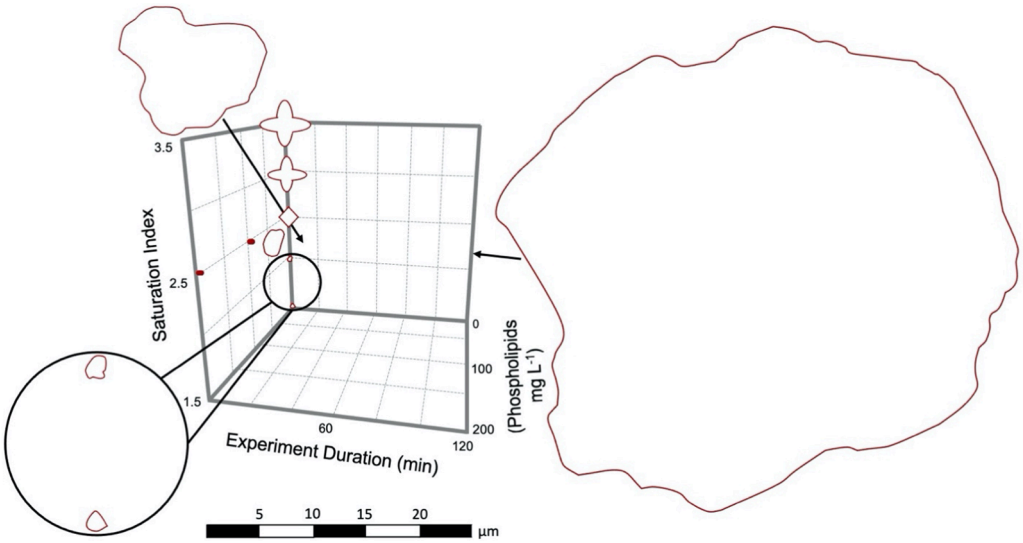

Fig. 7. Generalized schematic of characteristic barite size and morphology as a function of experimental barite saturation index, experiment duration, and soy phospholipid concentrations. Filled symbols indicate experimental conditions that yielded barite crystals that resemble marine barite.

may have still occurred via sulfate substitution into amorphous phosphorus-rich barite precursors that were rapidly replaced by crystalline barite under our experimental conditions. An amorphous phosphorus-rich barite precursor may contribute to the relatively high phosphorous counts observed via EDX for the Soy-100 treatment (Table SI). The morphological similarity between marine barite and barite precipitated in the presence of phospholipids in this investigation provides new evidence for this precipitation pathway occurring in marine organic matter aggregates.

Characteristic elliptical barite morphologies were only consistently observed in solutions with soy phospholipid concentrations above 10 mg L^{-1} (Fig. 4). This far exceeds reported phospholipid concentrations in seawater: e.g., 0.6–5.7 μg L^{-1} in the North Atlantic (Gašparović et al., 2018), 3.0–27.7 μg L^{-1} in the Mediterranean (Frka et al., 2011), and 36.4–93.5 μg L^{-1} in the Equatorial Atlantic (Triesch et al., 2021). Marine phospholipids are primarily observed within the cell membranes of bacteria and other organisms (Suzumura, 2005). Thus, phospholipid concentrations high enough to facilitate the precipitation of elliptical barite crystals may result from bacterial cell lysis, which can release cellular material into the extracellular matrix of organic matter aggregates (Flemming and Wingender, 2010). Phospholipids play a role in maintaining EPS structure (Wingender et al., 1999), so EPS microenvironments themselves may contain sufficient phospholipid concentrations to yield elliptical barite morphologies.

Phospholipid experiments produced elliptical morphologies like those most frequently observed in seawater, but these experiments did not produce the six-sided barite morphologies that are also observed in seawater and marine sediments (Fig. 1). Six-sided marine barite morphologies are likely produced by slightly different precipitation conditions than those recreated here. Godinho and Stack (2015) found that abiotic barite precipitation in the presence of NaCl favors the formation of six-sided crystals by promoting face-specific growth, and $SrCl_2$ can inhibit barite growth at particular crystal faces. Thus, six-sided marine barite crystals may form in the presence of relatively lower concentrations of organic compounds and reflect cation concentrations in their formation environments. These conditions warrant further study.

Lastly, our results suggest that marine barite precipitation is fairly rapid. Barite crystals from experiment durations of 10 min or more were more than twice the size and displayed more globular morphologies than typical marine barite crystals (Figs. 6, 7). This suggests that nascent barite crystals spend no more than a few minutes in microenvironments with a barite saturation index near 2.5. These supersaturated microenvironments themselves may be short-lived due to a depletion of Ba^{2+} or SO_4^{2-} ions. Alternatively, barite crystals may become dislodged from the precipitation microenvironment once they reach a certain size. Previous laboratory investigations simulating marine barite precipitation have conducted incubations on timescales of days or weeks (e.g., Ganeshram et al., 2003; González-Muñoz et al., 2003; Torres-Crespo et al., 2015). These relatively long time periods may be necessary to facilitate the formation of microenvironments supersaturated with respect to barite, but, once these microenvironments are formed, barite precipitation is likely much more rapid. Relatively few methods exist for studying microscale spatial and temporal variability within marine organic matter aggregates, so our findings provide valuable insights into their microscale heterogeneity and dynamism.

4.2. Crystallographic origins of different barite crystal morphologies

The different barite crystal morphologies observed here suggest differences in crystal structure and/or growth mechanisms between treatments. The larger size, globular morphology, and more polycrystalline SAED patterns observed for barite crystals with longer precipitation times suggest that they are the result of barite crystal aggregation. Alternatively, they may reflect the continued growth of existing barite particles once barite supersaturation has dropped below the threshold needed for the nucleation of new barite crystals (e.g., Weber et al., 2021).

Varied crystal morphology in the presence of organic additives may be partly due to heterogenous barite nucleation and growth, either on the glass walls of the beaker or, for phospholipid treatments, in association with microscopic phospholipid aggregates. Other investigations have observed Ba^{2+} accumulation and heterogeneous barite nucleation and growth at organic-water interfaces with terminal thiol (-SH) or carboxylic (-COOH) functional groups (Dai et al., 2016; Deng et al., 2022). As previously discussed, laboratory studies have also demonstrated that phospholipids concentrate Ba^{2+} (Martinez-Ruiz et al., 2018). This suggests that barite nucleation and growth may occur at organic-water interfaces with higher barite supersaturation than the surrounding solution in any of our experiments with organic additives. The texture of barite crystals synthesized in the presence of formic acid (Fig. 3A) somewhat resembled that of barite crystals formed in a solution with a barite saturation index of 3 (Fig. 2D), so localized Ba^{2+} accumulation and subsequent heterogeneous barite nucleation is particularly plausible for the formic acid treatment. Additional work is needed to assess heterogeneous barite nucleation and growth under conditions relevant to marine contexts.

The elliptical morphology observed for barite synthesized in the presence of EDTA is likely due to an increase in the relative exposure of particular crystal faces during crystallization. EDTA is an organic ligand that binds Ba^{2+}, but the influence of EDTA on barite morphology cannot be explained by complexation alone (Jones et al., 2007). Instead, Jones et al. (2007) suggests that EDTA influences barite morphology through carboxyl group interactions on positively charged Ba^{2+} ions at the (0,1,0) or (0,1,1) crystal faces. Our findings are consistent with this mechanism for crystal growth modification; d-spacings in the SAED pattern for a barite crystal synthesized in the presence of EDTA suggest a basal face of (0,1,1) (Fig. SIII).

Our findings and existing literature suggest some potential explanations for why phospholipid-bearing solutions produced elliptical barite crystals. Organic solvents can influence barite nucleation, step advancement rates, and Ba^{2+} desolvation (e.g., Jones et al., 2008; Kowacz et al., 2007; Piana et al., 2006), so the ethanol used to dissolve the soy phospholipids may have affected barite crystal growth in the soy phospholipid treatments. However, the experimental treatment with only ethanol produced rhomboidal crystals (Fig. 4A), so the elliptical crystals that formed in the presence of soy phospholipids were likely due to crystal nucleation or growth effects independent from the presence of an organic solvent. Similarly, while some phosphorus was observed within the phospholipid treatment barite crystals, EDX maps and spectra suggest that phosphorus abundance did not clearly correlate with crystal morphology or phospholipid concentrations in the precipitating solution (Fig. 4I, 4O, 4U, Table SI). This suggests that phospholipids do not primarily affect crystal morphology through direct incorporation into the barite crystal lattice but instead through one or more other mechanisms.

SAED patterns for crystals formed in the presence of soy phospholipids were insufficient to determine basal crystal faces with confidence (Fig. 4Q, 4W). However, given the similar crystal morphologies observed between soy phospholipid and EDTA treatments, it is plausible that carboxyl groups, phosphoryl groups, or other negatively charged phospholipid moieties influenced barite morphology via interactions at the (0,1,0) or (0,1,1) crystal faces, as is hypothesized to occur with EDTA. In fact, elliptical barite crystals and exposed (0,1,1) barite crystal faces were also observed in crystals precipitated in the presence of phosphonates (Black et al., 1991) and algae (Barbosa et al., 2022). The barite crystals grown with our phospholipid treatments displayed more irregular edges and yielded more poorly defined SAED patterns than EDTA treatment crystals (Figs. 3, 4). If phospholipid moiety interactions at barite crystal faces are responsible for the elliptical morphologies observed here, these irregularities suggest that phospholipid moieties are likely less consistent in their interactions with barite crystal faces than the carboxyl moieties of EDTA. This would be unsurprising, since phospholipids are larger and more structurally complex than EDTA.

Alternatively, phospholipids may create elliptical barite morphologies by causing the oriented aggregation of barite nanoparticles that form in association with phospholipid moieties. Elliptical barite morphologies in the presence of phytic acid are hypothesized to form via an interface coupled dissolution-precipitation mechanism in which an amorphous Ba-P phase is replaced with crystalline barite sub-units that aggregate with a preferential orientation (Ruiz Agudo et al., 2021). Similar aggregation pathways have been proposed for barite precipitation in the presence of other polymers and solvents (Fillingham et al., 2021; Qi et al., 2001; Ruiz-Agudo et al., 2020). Nonclassical crystallization by particle attachment and the transition from amorphous precursor to crystalline substance is common in the biomineralization of minerals such as calcite, magnetite, and zeolite (Jones and Ogden, 2009; De Yoreo et al., 2015 and references therein). Therefore, nonclassical crystallization pathways such as oriented aggregation may contribute to the elliptical barite morphologies observed here and in marine barite.

Lastly, elliptical barite morphologies may have been promoted by the viscosity of microenvironments within the soy phospholipid treatments. Previous work has shown that viscous media and microbial EPS promotes the formation of rounded calcium carbonate crystal morphologies by slowing the rate of ion diffusion and thus the rate of precipitation (Braissant et al., 2003; Buczynski and Chafetz, 1991; Chekroun et al., 2004). Phospholipids increase the viscosity of a solution (Schneider, 1997). Modeling and experimental work suggests that Ba^{2+} desolvation from water is the rate-limiting step in barite precipitation (Piana et al., 2006; Stack et al., 2016). Phospholipids may, in part, modify barite crystal morphology by influencing Ba^{2+} diffusion and/or desolvation and thus face-specific growth rates.

4.3. Implications for the marine barite proxy

Barite has been extensively used as a proxy for past ocean conditions (e.g., Carter et al., 2016; Erhardt et al., 2013; Kim et al., 2022; Lowery and Bralower, 2022; Ma et al., 2014; Paytan et al., 1996), but its utility is limited by uncertainties surrounding barite formation, precipitation, dissolution, and variation in time and space (e.g., Carter et al., 2020). Our work advances the barite proxy by 1) developing methods that facilitate future laboratory investigations into marine barite dynamics and 2) providing evidence for marine barite as an ecosystem-wide proxy for export production.

Here, we developed simple and reliable methods for the synthesis of crystals resembling marine barite in size and shape. Laboratory investigations into marine barite dynamics have been lacking. Notably, we find that high barite saturation indices at solution mixing interfaces are an obstacle to simulating marine barite precipitation. As we discuss in our Methods section, this obstacle can be overcome and model marine barite crystals can be synthesized through the addition of dilute Na_2SO_4 to a relatively large volume of rapidly stirred artificial seawater containing Ba^{2+} and either EDTA or soy phospholipids. This method can be used to create barite crystals for future laboratory-based investigations into processes such as marine barite dissolution, ballasting of organic matter aggregates, and isotopic fractionation.

Our experiments also shed light onto marine barite precipitation mechanisms. Previous work suggested that elliptical marine barite crystals are the result of biotic precipitation within vesicles (Bertram and Cowen, 1997), but our findings demonstrate that this characteristic marine barite morphology can precipitate without direct biological mediation. Rather, we find that crystals resembling marine barite in size and morphology passively precipitate in synthetic seawater with high concentrations of naturally occurring phospholipids. As previously discussed, this is consistent with the hypothesis that phospholipids within marine EPS facilitate barium accumulation and marine barite precipitation (Martinez-Ruiz et al., 2018, 2019). The fundamentally abiotic, passive precipitation of marine barite in association with chemical gradients created by biological activity and organic matter remineralization strengthens marine barite's utility as a proxy. It suggests that marine barite accumulation rates are not dependent on particular organism types but instead on EPS, which are produced by most marine microbes (Decho and Gutierrez, 2017). Thus, barite is likely to serve as an ecosystem-wide productivity proxy.

5. Conclusions

Here, we used barite crystal morphology to constrain the plausible biogeochemical conditions under which marine barite precipitates. Our findings are consistent with the role of phospholipids in marine barite precipitation and provide new insight into microenvironments within marine organic matter aggregates. We suggest that marine barite is likely to crystallize quickly (within a few minutes or less) and at saturation indices near 2.5. The brief experiment durations needed to form crystals resembling marine barite suggest that the precipitation conditions for marine barite are ephemeral, perhaps reflecting the rapid drawdown of saturation state as crystallization occurs. Moreover, we have facilitated future laboratory investigations into marine barite dynamics by developing simple and reliable methods for the synthesis of crystals that resemble marine barite in size and shape. These efforts advance marine barite as a tool for studying the marine carbon cycle in the past and present. This work also contributes to our understanding of mineral nucleation and growth within the ocean, biofilms, and other natural systems.

Declaration of Competing Interest

The authors declare that they have no known competing financial interests or personal relationships that could have appeared to influence the work reported in this paper.

Acknowledgements

T.L. was supported by a U.S. Department of Defense National Defense Science and Engineering Graduate Student Fellowship, a William B. and Dorothy Heroy Research Grant from the Geological Society of America, and a Ruth Newmark Scholarship from the UCSD Friends of the International Center. The authors thank Drs. Athina Lange, Julia Diaz, Adina Paytan, and Tristan Horner for their valuable insights.

Appendix A. Supplementary material

The attached files provide additional data supporting the conclusions presented in this manuscript. We show SEM images of barite crystals precipitated under different Ba^{2+}:Sr^{2+} and Ba^{2+}:SO_4^{2-} ratios. We present semi-quantitative analyses of relative phosphorous intensities for soy phospholipid treatments. We also present CrysTBox indexing analysis results for a SAED pattern of a barite crystal synthesized in the presence of EDTA. Lastly, we provide the microcrystal size observations that underlie Fig. 6. Supplementary material to this article can be found online at https://doi.org/10.1016/j.gca.2023.08.012.

References

Akyol, E., Cedimagar, M.A., 2016. Size and morphology controlled synthesis of barium sulfate. Cryst. Res. Tech. 51, 393–399.

Arganda-Carreras, I., Kaynig, V., Rueden, C., Eliceiri, K.W., Schindelin, J., Cardona, A., Seung, S.H., 2017. Trainable Weka segmentation: A machine learning tool for microscopy pixel classification. Bioinformatics 33, 2424–3246.

Barbosa, N., Jaquet, J., Urquidi, O., Adachi, T.B.M., Filella, M., 2022. Combined in vitro and in vivo investigation of barite microcrystals in *Spirogyra* (Zygnematophyceae, Charophyta). J. Plant Physiol. 276, 153769.

Benton, W.J., Collins, I.R., Grimsey, I.M., Parkinson, G.M., Rodger, S.A., 1993. Nucleation, growth and inhibition of barium sulfate-controlled modification with organic and inorganic additives. Faraday Discuss. 95, 281.

Bernard-Michel, B., Pons, M.N., Vivier, H., 2002. Quantification, by image analysis, of effect of operational conditions on size and shape of precipitated barium sulphate. Chem. Eng. J. 87, 135–147.

Bertram, M.A., Cowen, J.P., 1997. Morphological and compositional evidence for biotic precipitation of marine barite. J. Mar. Res. 55, 577–593.
Bethke, C.M., 2022. Geochemical and Biogeochemical Reaction Modeling. Cambridge University Press, Cambridge.
Bishop, J.K.B., 1988. The barite-opal-organic carbon association in oceanic particulate matter. Nature 332, 341.
Black, S.N., Bromley, L.A., Cottier, D., Davey, R.J., Dobbs, B., 1991. Interactions at the organic/inorganic interface: binding motifs for phosphonates at the surface of barite crystals. J. Chem. Soc. Faraday Trans. 87, 6.
Boon, M., Jones, F., 2016. Barium sulfate crystallization from synthetic seawater. Crys. Growth Des. 16, 4646–4657.
Bracco, J.N., Gooijer, Y., Higgins, S.R., 2016. Hydrothermal atomic force microscopy observations of barite step growth rates as a function of the aqueous barium-to-sulfate ratio. Geochim. Cosmochim. Acta 183, 1–13.
Braissant, O., Cailleau, G., Dupraz, C., Verrecchia, E.P., 2003. Bacterially induced mineralization of calcium carbonate in terrestrial environments: the role of exopolysaccharides and amino acids. J. Sed. Res. 73, 485–490.
Buczynski, C., Chafetz, H.S., 1991. Habit of bacterially induced precipitates of calcium carbonate and the influence of medium viscosity on mineralogy. J. Sed. Res. 61, 226–233.
Buesseler, K.O., Boyd, P.W., Black, E.E., Siegel, D.A., 2020. Metrics that matter for assessing the ocean biological carbon pump. Proc. Natl. Acad. Sci. 117, 9679–9687.
Carter, S.C., Griffith, E.M., Penman, D.E., 2016. Peak intervals of equatorial Pacific export production during the middle Miocene climate transition. Geology 44, 923–926.
Carter, S.C., Paytan, A., Griffith, E.M., 2020. Toward an improved understanding of the marine barium cycle and the application of marine barite as a paleoproductivity proxy. Minerals. 10, 421.
Chekroun, K.B., Rodríguez-Navarro, C., González-Muñoz, M.T., Arias, J.M., Cultrone, G., Rodríguez-Gallego, M., 2004. Precipitation and growth morphology of calcium carbonate induced by Myxococcus xanthus: implications for recognition of bacterial carbonates. J. Sed. Res. 74, 868–876.
Dai, C., Stack, A.G., Koishi, A., Fernandez-Martinez, A., Lee, S.S., Hu, Y., 2016. Heterogeneous nucleation and growth of barium sulfate at organic–water interfaces: interplay between surface hydrophobicity and Ba2+ adsorption. Langmuir 32, 5277–5284.
De Yoreo, J.J., Gilbert, P.U., Sommerdijk, N.A., Penn, R.L., Whitelam, S., Joester, D., Zhang, H., Rimer, J.D., Navrotsky, A., Banfield, J.F., Wallace, A.F., Marc Michelle, F., Meldrum, F.C., Cölfen, H., Dove, P.M., 2015. Crystallization by particle attachment in synthetic, biogenic, and geologic environments. Science 349, aaa6760.
Decho, A.W., Gutierrez, T., 2017. Microbial extracellular polymeric substances (EPSs) in ocean systems. Front. Microbiol. 8, 922.
Dehairs, F., Chesselet, R., Jedwab, J., 1980. Discrete suspended particles of barite and the barium cycle in the open ocean. Earth Planet. Sci. Lett. 49, 528–550.
Deng, N., Stack, A.G., Weber, J., Cao, B., De Yoreo, J.J., Hu, Y., 2019. Organic–mineral interfacial chemistry drives heterogeneous nucleation of Sr-rich (Ba_x, Sr_{1-x}) SO_4 from undersaturated solution. Proc. Nat. Acad. Sci. 116, 13221–13226.
Deng, N., Zuo, X., Stack, A.G., Lee, S.S., Zhou, Z., Weber, J., Hu, Y., 2022. Selenite and selenate sequestration during coprecipitation with barite: insights from mineralization processes of adsorption, nucleation, and growth. Environ. Sci. Tech. 56, 15518–15527.
Dirksen, J.A., Ring, T.A., 1991. Fundamentals of crystallization: kinetic effects on particle size distributions and morphology. Chem. Eng. Sci. 46, 2389–2427.
Dupraz, C., Reid, R.P., Braissant, O., Decho, A.W., Norman, R.S., Visscher, P.T., 2009. Processes of carbonate precipitation in modern microbial mats. Earth Sci. Rev. 96, 141–162.
Emerson, S., Hedges, J., 2008. Chemical Oceanography and the Marine Carbon Cycle. Cambridge University Press, Cambridge.
Erhardt, A.M., Pälike, H., Paytan, A., 2013. High-resolution record of export production in the eastern equatorial Pacific across the Eocene-Oligocene transition and relationships to global climatic records. Paleoceanography 28, 130–142.
Fakhraee, M., Planavsky, N.J., Reinhard, C.T., 2020. The role of environmental factors in the long-term evolution of the marine biological pump. Nat. Geosci. 13, 812–886.
Fernandez-Diaz, L., Putnis, A., Cumberbatch, T.J., 1990. Barite nucleation kinetics and the effect of additives. Eur. J. Mineral. 2, 495–502.
Fillingham, R., Boon, M., Javaid, S., Saunders, J.A., Jones, F., 2021. Barium sulfate crystallization in non-aqueous solvent. Cryst. Eng. Comm. 23, 2249–2261.
Flemming, H., Wingender, J., 2010. The biofilm matrix. Nat. Rev. Microbiol. 8, 623–633.
Freeman, S.R., Jones, F., Ogden, M.I., Oliviera, A., Richmond, W.R., 2006. Effect of benzoic acids on barite and calcite precipitation. Cryst. Growth Des. 6, 2579–2587.
Frka, S., Gašparović, B., Marić, D., Godrijan, J., Djakovac, T., Vojvodić, V., Dautović, J., Kozarac, Z., 2011. Phytoplankton driven distribution of dissolved and particulate lipids in a semi-enclosed temperate sea (Mediterranean): spring to summer situation. Estuar. Coast. Shelf Sci. 93, 290–304.
Ganeshram, R.S., François, R., Commeau, J., Brown-Leger, S.L., 2003. An experimental investigation of barite formation in seawater. Geochim. Cosmochim. Acta 67, 2599–2605.
Garcia-Ruiz, J., 1999. Morphological behavior of inorganic precipitation systems. Inst. Met. Mis. Astrobiol. II. 3755, 74–82.
Gašparović, B., Penezić, A., Lampitt, R.S., Sudasinghe, N., Schaub, T., 2018. Phospholipids as a component of the oceanic phosphorus cycle. Mar. Chem. 205, 70–80.
Godinho, J.R., Stack, A.G., 2015. Growth kinetics and morphology of barite crystals derived from face-specific growth rates. Cryst. Growth Des. 15, 2064–2071.
Goldschmidt, V.M., 1913. Atlas der Krystallformen. Carl Winters Universitätsbuchhandlung, Heidelberg.
González-Muñoz, M.T., Fernández-Luque, B., Martínez-Ruiz, F., Chekroun, K.B., Arias, J. M., Rodríguez-Gallego, M., Martínez-Cañamero, M., de Linares, C., Paytan, A., 2003. Precipitation of barite by *Myxococcus Xanthus*: possible implications for the biogeochemical cycle of barium. Appl. Environ. Microbiol. 69, 5722–6575.
Griffith, E.M., Thomas, E., Lewis, A.R., Penman, D.E., Westerhold, T., Winguth, A.M.E., 2021. Bentho-pelagic decoupling: the marine biological carbon pump during eocene hyperthermals. Paleoceanogr. Paleoclimatol. 36 e2020PA004053.
He, S., Oddo, J.E., Tomson, M.B., 1995. The nucleation kinetics of barium sulfate in NaCl solutions up to 6 m and 90 C. J. Colloid Interf. Sci. 174, 319–326.
Henson, S.A., Laufkötter, C., Leung, S., Giering, S.L.C., Palevsky, H.I., Cavan, E.L., 2022. Uncertain response of ocean biological carbon export in a changing world. Nat. Geosci. 15, 248–254.
House, B.M., Norris, R.D., 2020. Unlocking the barite paleoproductivity proxy: A new high-throughput method for quantifying barite in marine sediments. Chem. Geo. 552, 119664.
Hsieh, Y., Henderson, G.M., 2017. Barium stable isotopes in the global ocean: tracer of Ba inputs and utilization. Earth Planet. Sci. Lett. 473, 269–278.
Hülse, D., Arndt, S., Wilson, J.D., Munhoven, G., Ridgwell, A., 2017. Understanding the causes and consequences of past marine carbon cycling variability through models. Earth Sci. Rev. 171, 349–382.
Iversen, M.H., 2023. Carbon export in the ocean: A biologist's perspective. Ann. Rev. Mar. Sci. 15, 357–381.
Jacquet, S.H.M., Dehairs, F., Dumont, I., Becquevort, S., Cavagna, A.J., Cardinal, D., 2011. Twilight zone organic carbon remineralization in the polar front zone and subantarctic Zone South of Tasmania. Deep Sea Res. II: Top Stud. Oceanogr. 58, 2222–2234.
Jones, F., 2012. Infrared investigation of barite and gypsum crystallization: Evidence for an amorphous to crystalline transition. CrstEngComm 14, 8374–8381.
Jones, F., Ogden, M.I., 2009. Controlling crystal growth with modifiers. CrstEngComm 12, 1016–1023.
Jones, F., Jones, P., Ogden, M.I., Richmond, W.R., Rohl, A.L., Saunders, M., 2007. The interaction of EDTA with barium sulfate. J. Colloid Interface Sci. 316, 553–561.
Jones, F., Piana, S., Gale, J.D., 2008. Understanding the kinetics of barium sulfate precipitation from water and water–methanol solutions. Cryst. Growth Des. 8, 817–822.
Judat, B., Kind, M., 2004. Morphology and internal structure of barium sulfate—derivation of a new growth mechanism. J. Colloid Interface Sci. 269, 341–353.
Kim, J.E., Westerhold, T., Alegret, L., Drury, A.J., Röhl, U., Griffith, E.M., 2022. Precessional pacing of tropical ocean carbon export during the Late Cretaceous. Clim. Past 18, 2631–2641.
Klinger, M., 2017. More features, more tools, more CrysTBox. J. Appl. Cryst. 50, 1226–1234.
Kowacz, M., Putnis, C.V., Putnis, A., 2007. The effect of cation: anion ratio in solution on the mechanism of barite growth at constant supersaturation: Role of the desolvation process on the growth kinetics. Geochim. Cosmochim. Acta 71, 5168–5179.
Koyama, T., Thompson, T.G., 1964. Identification and determination of organic acids in sea water by partition chromatography. J. Oceanogr. Soc. Japan 20, 209–220.
Kucher, M., Babic, D., Kind, M., 2006. Precipitation of barium sulfate: experimental investigation about the influence of supersaturation and free lattice ion ratio on particle formation. Chem. Eng. Process. 45, 900–907.
Light, T., Norris, R., 2021. Quantitative visual analysis of marine barite microcrystals: insights into precipitation and dissolution dynamics. Limnol. Oceanogr. 66, 3619–3629.
Liu, Y., Guo, X., Yang, S., He, Q., Jin, H., 2018. Controllable preparation of uniform micron-sized barium-sulfate spheres. Cryst. Res. Tech. 53, 1700212.
Liu, S., Parsons, R., Opalk, K., Baetge, N., Giovannoni, S., Bolaños, L.M., Kujawinski, E.B., Longnecker, K., Lu, Y., Halewood, E., Carlson, C.A., 2020. Different carboxyl-rich alicyclic molecules proxy compounds select distinct bacterioplankton for oxidation of dissolved organic matter in the mesopelagic Sargasso Sea. Limnol. Oceanogr.. 65, 1532–1553.
Lowery, C.M., Bralower, T.J., 2022. Elevated post K-Pg export productivity in the Gulf of Mexico and caribbean. Paleoceanogr. Paleoclim. 37 e2021PA004400.
Ma, Z., Gray, E., Thomas, E., Murphy, B., Zachos, J., Paytan, A., 2014. Carbon sequestration during the Palaeocene-Eocene thermal maximum by an efficient biological pump. Nat. Geosci. 7, 382–438.
Markovic, S., Paytan, A., Li, H., Wortmann, U.G., 2016. A revised seawater sulfate oxygen isotope record for the last 4Myr. Geochim. Cosmochim. Acta 175, 239–251.
Martinez-Ruiz, F., Jroundi, F., Paytan, A., Guerra-Tschuschke, I., Abad, M., González-Muñoz, M.T., 2018. Barium bioaccumulation by bacterial biofilms and implications for Ba cycling and use of Ba proxies. Nat. Comm. 9, 1619.
Martinez-Ruiz, F., Paytan, A., Gonzalez-Muñoz, M.T., Jroundi, F., Abad, M.M., Lam, P.J., Bishop, J.K.B., Horner, T.J., Morton, P.L., Kastner, M., 2019. Barite formation in the ocean: origin of amorphous and crystalline precipitates. Chem. Geol. 511, 441–451.
Martinez-Ruiz, F., Paytan, A., Gonzalez-Muñoz, M.T., Jroundi, F., Abad, M.M., Lam, P.J., Horner, T.J., Kastner, M., 2020. Barite precipitation on suspended organic matter in the mesopelagic zone. Front. Earth Sci. 8, 567714.
Monnin, C., Jeandel, C., Cattaldo, T., Dehairs, F., 1999. The Marine barite saturation state of the world's oceans. Mar. Chem. 65, 253–261.
Murray, R.W., Leinen, M., 1993. Chemical transport to the seafloor of the equatorial Pacific Ocean across a latitudinal transect at 135 W: tracking sedimentary major, trace, and rare earth element fluxes at the Equator and the Intertropical Convergence Zone. Geochim. Comochim. Acta. 57, 4141–4163.
Nowicki, M., DeVries, T., Siegel, D.A., 2022. Quantifying the carbon export and sequestration pathways of the ocean's biological carbon pump. Glob. Biogeochem. Cycles. 36 e2021GB007083.

Oviedo, C., Rodríguez, J., 2003. EDTA: the chelating agent under environmental scrutiny. Quim. Nova 26, 901–905.
Paytan, A., Kastner, M., Martin, E.E., Macdougall, J.D., Herbert, T., 1993. Marine barite as a monitor of seawater strontium isotope composition. Nature 366, 445–449.
Paytan, A., Kastner, M., Chavez, F.P., 1996. Glacial to interglacial fluctuations in productivity in the equatorial Pacific as indicated by marine barite. Science 274, 1355–1357.
Paytan, A., Kastner, M., Campbell, D., Thiemens, M.H., 1998. Sulfur isotopic composition of cenozoic seawater sulfate. Science 282, 1459–1462.
Piana, S., Jones, F., Gale, J.D., 2006. Assisted desolvation as a key kinetic step for crystal growth. J. Am. Chem. Soc. 128, 13568–13574.
Qi, L., Cölfen, H., Antonietti, M., Li, M., Hopwood, J.D., Ashley, A.J., Mann, S., 2001. Formation of $BaSO_4$ fibres with morphological complexity in aqueous polymer solutions. Chem Eur J 7, 3526–3532.
R Core Team, 2020. R: A Language and Environment for Statistical Computing. R Foundation for Statistical Computing, Vienna, Austria.
Ruiz Agudo, C., Ibañez-Velasco, A., Ruiz-Agudo, E., 2021. The role of amorphous P-bearing precursors on barite formation. Geochem. Perspect. Lett. 18, 32–36.
Ruiz-Agudo, C., Ruiz-Agudo, E., Putnis, C.V., Putnis, A., 2015. Mechanistic principles of barite formation: from nanoparticles to micron-sized crystals. Cryst. Growth Des. 15, 3724–3733.
Ruiz-Agudo, C., Ruiz-Agudo, E., Burgos-Cara, A., Putnis, C.V., Ibáñez-Velasco, A., Rodriguez-Navarro, C., Putnis, A., 2016. Exploring the effect of poly(acrylic acid) on pre-and post-nucleation $BaSO_4$ species: New insights into the mechanisms of crystallization control by polyelectrolytes. CrstEngComm 18, 2830–2842.
Ruiz-Agudo, C., McDonogh, D., Avaro, J.T., Schupp, D.J., Gebauer, D., 2020. Capturing an amorphous $BaSO_4$ intermediate precursor to barite. CrstEngComm 22, 1310–1313.
Sánchez-Pastor, N., Pina, C.M., Fernandez-Diaz, L., 2006. Relationships between crystal morphology and composition in the (Ba, Sr) SO_4–H_2O solid solution–aqueous solution system. Chem. Geo. 225, 266–277.
Saraya, M.E.S.I., 2015. Effect of L (+) ascorbic acid and monosodium glutamate concentration on the morphology of calcium carbonate. J. Solid State Chem. 231, 114–122.
Schindelin, J., Arganda-Carreras, I., Frise, E., Kaynig, V., Longair, M., Pietzsch, T., Preibisch, S., et al., 2012. Fiji: An open-source platform for biological-image analysis. Nat. Methods 9, 676–682.
Schindelin, J., Rueden, C.T., Hiner, M.C., Eliceiri, K.W., 2015. The ImageJ ecosystem: an open platform for biomedical image analysis. Mol. Reprod. Dev 82, 518–529.
Schneider, M., 1997. Phospholipids. In: Gunstone, F.D., Padley, F.B. (Eds.), Lipid Technologies and Applications. Routledge, Milton Park, pp. 51–78.
Shen, Y., Li, C., Zhu, X., Xie, A., Qiu, L., Zhu, J., 2007. Study on the preparation and formation mechanism of barium sulphate nanoparticles modified by different organic acids. J. Chem. Sci. 119, 319–324.
Smith, E., Hamilton-Taylor, J., Davison, W., Fullwood, N.J., McGrath, M., 2004. The effect of humic substances on barite precipitation–dissolution behaviour in natural and synthetic lake waters. Chem. Geo. 207, 81–89.
Stack, A.G., Borreguero, J.M., Prisk, T.R., Mamontov, E., Wang, H.W., Vlcek, L., Wesolowski, D.J., 2016. Precise determination of water exchanges on a mineral surface. Phys. Chem. Chem. Phys. 18, 28819–28828.
Sun, X., Yang, Z., Fan, D., Li, Y., 2015. Crystals of suspended marine barite in the eastern equatorial pacific: processes of dissolution and effects on crystal morphology. Chin. J. Oceanol. Limnol. 33, 194–203.
Suzumura, M., 2005. Phospholipids in marine environments: A review. Talanta 66, 422–434.
Torres-Crespo, N., Martínez-Ruiz, F., González-Muñoz, M.T., Bedmar, E.J., De Lange, G. J., Jroundi, G.J., 2015. Role of bacteria in marine barite precipitation: A case study using Mediterranean seawater. Sci. Tot. Environ. 512–513, 562–571.
Triesch, N., van Pinxteren, M., Frka, S., Stolle, C., Spranger, T., Hoffmann, E.H., Gong, X., et al., 2021. Concerted measurements of lipids in seawater and on submicrometer aerosol particles at the Cabo Verde Islands: biogenic sources, selective transfer and high enrichments. Atmospheric Chem. Phys. 21, 4267–4283.
Wangersky, P.J., 1952. Isolation of ascorbic acid and rhamnosides from sea water. Science 115, 685.
Weber, J., Bracco, J.N., Poplawsky, J.D., Ievlev, A.V., More, K.L., Lorenz, M., Bertagni, A. L., Jindra, S.A., Starchenko, V., Higgins, S.R., Stack, A.G., 2018. Unraveling the effects of strontium incorporation on barite growth—In situ and ex situ observations using multiscale chemical imaging. Cryst. Growth Des. 18, 5521–5533.
Weber, J., Bracco, J.N., Yuan, K., Starchenko, V., Stack, A.G., 2021. Studies of mineral nucleation and growth across multiple scales: review of the current State of research using the example of barite ($BaSO_4$). ACS Earth Space Chem. 5, 3338–3361.
Wickham, H., 2016. Ggplot2: Elegant Graphics for Data Analysis. Springer-Verlag, New York.
Widanagamage, I.H., Schauble, E.A., Scher, H.D., Griffith, E.M., 2014. Stable strontium isotope fractionation in synthetic barite. Geochim. Chosmochim. Acta. 147, 58–75.
Widanagamage, I.H., Waldron, A.R., Glamoclija, M., 2018. Controls on barite crystal morphology during abiotic precipitation. Minerals 8, 480.
Wingender, J., Neu, T.R., Flemming, H., 1999. What Are Bacterial Extracellular Polymeric Substances? In: Wingender, J., Neu, T.R., Flemming, H. (Eds.), Microbial Extracellular Polymeric Substances: Characterization, Structure and Function. Springer, Berlin, pp. 1–19.
Yao, W., Paytan, A., Griffith, E.M., Martínez-Ruiz, F., Markovic, S., Wortmann, U.G., 2020. A revised seawater sulfate S-isotope curve for the eocene. Chem. Geol. 532, 119382.
Yao, W., Griffith, E., Paytan, A., 2021. Pelagic Barite: Tracer of Ocean Productivity and a Recorder of Isotopic Compositions of Seawater S, O, Sr, Ca and Ba, 1st ed. Cambridge University Press, Cambridge.
Yuan, K., Starchenko, V., Rampal, N., Yang, F., Yang, X., Xiao, X., Lee, W.K., Stack, A.G., 2021. Opposing effects of impurity ion Sr2+ on the heterogeneous nucleation and growth of barite ($BaSO_4$). Cryst. Growth Des. 21, 5828–5839.
Zhang, M., Zhang, B., Li, X., Yin, Z., Guo, X., 2011. Synthesis and surface properties of submicron barium sulfate particles. Appl. Surf. Sci. 258, 24–29.